

2011

Nonuniformity in Lattice Contraction of Bismuth Nanoclusters Heated Near Its Melting Point

A. Esmail

Old Dominion University


M. Abdel-Fattah

Old Dominion University

Hani E. Elsayed-Ali

Old Dominion University, helsayed@odu.edu

Follow this and additional works at: https://digitalcommons.odu.edu/ece_fac_pubs

 Part of the [Materials Science and Engineering Commons](#), [Nanoscience and Nanotechnology Commons](#), [Optics Commons](#), and the [Physical Chemistry Commons](#)

Repository Citation

Esmail, A.; Abdel-Fattah, M.; and Elsayed-Ali, Hani E., "Nonuniformity in Lattice Contraction of Bismuth Nanoclusters Heated Near Its Melting Point" (2011). *Electrical & Computer Engineering Faculty Publications*. 98.
https://digitalcommons.odu.edu/ece_fac_pubs/98

Original Publication Citation

Esmail, A., Abdel-Fattah, M., & Elsayed-Ali, H. E. (2011). Nonuniformity in lattice contraction of bismuth nanoclusters heated near its melting point. *Journal of Applied Physics*, 109(8), 084317. doi:10.1063/1.3565028

Nonuniformity in lattice contraction of bismuth nanoclusters heated near its melting point

A. Esmail, M. Abdel-Fattah, and H. E. Elsayed-Ali^{a)}

Department of Electrical and Computer Engineering and the Applied Research Center, Old Dominion University, Norfolk, Virginia 23529, USA

(Received 10 November 2010; accepted 17 February 2011; published online 20 April 2011)

The structural properties of bismuth nanoclusters were investigated with transmission high-energy electron diffraction from room temperature up to 525 ± 6 K. The Bi nanoclusters were fabricated by thermal evaporation at room temperature on transmission electron microscope grids coated with an ultrathin carbon film, followed by thermal and femtosecond laser annealing. The annealed sample had an average cluster size of ~ 14 nm along the minor axis and ~ 16 nm along the major axis. The Debye temperature of the annealed nanoclusters was found to be 53 ± 6 K along the [012] direction and 86 ± 9 K along the [110] direction. At $T = 464 \pm 6$ K, the diffraction intensity started to deviate from Debye–Waller behavior due to increased lattice anharmonicity. The onset of the melting of the Bi nanoclusters was $T \sim 500 \pm 6$ K, as measured by the reduction of the nanocluster size through the formation of a liquid shell detected by the width of the diffraction rings. The thermal expansion coefficient of the Bi (012) and (110) planes is positive up to $\sim 499 \pm 11$ K. However, the expansion coefficient of the Bi (012) planes showed a transition from a positive to a negative value that occurs over the temperature range $T_c \sim 499 \pm 11$ K to 511 ± 8 K. For the Bi (110) planes, the thermal expansion coefficient is positive up to their melting point, which is 525 ± 6 K. © 2011 American Institute of Physics. [doi:10.1063/1.3565028]

I. INTRODUCTION

The chemical and physical properties of a substance are greatly affected when its size is reduced to the nanometer scale. Melting point depression as a result of size reduction is widely observed.^{1,2} This phenomenon results from the increase in the number of the surface atoms at the expense of the core atoms as the size of a particle is reduced to the nanoscale.

At least three different models were proposed to account for melting of small particles: the homogeneous melting model with no liquid shell formation,³ the liquid shell model,^{4–6} and the liquid nucleation model with liquid shell formation.^{7–10} These models show the inverse relation between the particle size and its melting temperature.¹¹ This behavior was confirmed experimentally in many elements, including gold,^{12,13} lead,¹¹ and bismuth.^{14–18}

The elastic properties of nanoclusters also show dependence on the cluster size. The magnitude of the thermal expansion coefficient was found to have inverse relation with the cluster size for some elements, e.g., copper¹⁹ and selenium,²⁰ and remains constant for some other elements, e.g., palladium.²⁰ Another study showed that palladium nanoclusters have the same behavior as copper and selenium nanoclusters.²¹ Other factors that affect the physical properties of the nanoclusters are their morphology and history of heat treatment.^{20,22}

Bulk Bi is semimetallic with small overlap of 38 meV between the conduction and valence bands.²³ As the size of Bi clusters was reduced to the nanometer scale, a transition

from semimetal with small overlap between the conduction and valence bands to a semiconductor of indirect bandgap was observed at a critical thickness of 49 nm at 77 K and 13 nm at 293 K.^{24,25}

Bulk Bi normally has a rhombohedral structure at ambient conditions. However, Bi is a polymorphic material that exhibits a solid–solid phase transition at high pressures and temperatures.^{26,27} The rhombohedral structure of Bi may be visualized as a distorted, simple cubic unit cell with two atoms per unit cell and lattice parameters of $a_{rh} = 4.7459$ Å, $\alpha_{rh} = 57^\circ 14.2'$.²⁸ One of the two atoms is located at the corner and the other at $(2u, 2u, 2u)$, where $u = 0.237$ Å.²⁸ This lattice distortion is considered to be responsible for the semimetallic behavior of Bi.²⁹ Bi can also be visualized as having a pseudo-cubic or hexagonal structure.^{30,31} Bi has a relatively low bulk melting point, $T_{bm} = 544$ K, and is known to undergo negative volume change upon melting.^{17,18,32} A transition from positive to negative thermal expansion was observed for Bi nanowires that are highly oriented along the [110] direction. This transition temperature was directly proportional to the nanowire diameter and was attributed to the effect of valence electron potential on the equilibrium lattice separation.³³

In the present study, transmission high-energy electron diffraction (THEED) was used to study the thermal expansion of annealed Bi nanoclusters from room temperature up to 525 ± 6 K. This was accomplished by monitoring their diffraction pattern as a function of temperature. The Bi nanoclusters were fabricated by thermal evaporation, followed by annealing thermally on a heated stage and by femtosecond laser pulses.

The temperature-dependent Bragg peak intensity and ring position, as well as the diffraction full width at half

^{a)}Author to whom correspondence should be addressed. Electronic mail: helsayed@odu.edu. Fax: (757)683-3220.

maximum (FWHM) were monitored for the (012) and (110) Bragg peaks. High-resolution transmission electron microscopy (TEM) was also used to characterize the as-evaporated and the annealed Bi nanoclusters.

II. EXPERIMENT

Bi noncontinuous film of 5 nm average thickness was grown by thermal evaporation on 3 mm copper TEM grids coated with <10-nm-thick carbon layer. Bi chunks (99.999% pure) were loaded into a tungsten boat. The base pressure of the evaporation chamber was in the low 10^{-6} Torr range. The evaporation rate was controlled by varying the current through the tungsten boat. A quartz crystal thickness monitor was used to measure the deposition rate and thickness. Evaporation was done at room temperature at a rate of $\sim 0.5 \text{ \AA s}^{-1}$.

A transmission electron diffraction system, built in our lab, was used to study the melting of the Bi nanoclusters. The diffraction patterns were obtained over the temperature range of $300 \pm 6 \text{ K}$ – $525 \pm 6 \text{ K}$. The THEED system is operated in an ultrahigh vacuum chamber (low 10^{-9} Torr). The 35 keV photoactivated electron gun, used in electron diffraction, is capable of generating a well-collimated electron beam with beam diameter of $745 \pm 54 \text{ \mu m}$, measured at the sample location. A microchannel plate followed by a phosphorous screen is used for diffraction pattern detection, and a computer-controlled, charge-coupled device camera is used to capture the diffraction pattern for analysis. The electron beam was steered toward the sample by a set of electromagnets located outside the ultrahigh vacuum chamber. Laser pulses from a 120 fs Ti:sapphire laser, operated at a wavelength of 800 nm and at a frequency of 1 kHz, was used for nanocluster annealing.

The samples were mounted on a lab-made heating stage designed to operate in the transmission diffraction system. For temperature measurements, we used a *K*-type thermocouple that was mounted inside the heater, about 1–2 mm away from the sample. The thermocouple was put through a calibration procedure to accurately measure the sample temperature. This was done by measuring the boiling point and the freezing point of distilled water and the melting point of a small Bi chunk. The temperature measurement accuracy was $\pm 1 \text{ K}$.

The as-deposited Bi sample was heated from room temperature up to 450 K with a heating rate of $\sim 3 \text{ K/min}$ while exposing the sample to femtosecond laser pulses with a fluence of $\sim 0.8 \text{ mJ/cm}^2$. At 450 K, the sample was further heated by the laser pulses for about 20 s with the laser operating at 1 kHz repetition rate. This resulted in the melting of the as-deposited Bi film and its quenching to form Bi nanoclusters.

III. RESULTS AND DISCUSSION

A. Morphology and diffraction pattern indexing of the grown bismuth nanoclusters

The fabricated Bi nanoclusters were studied by THEED and high-resolution TEM. Figure 1 shows the diffraction pattern and the TEM images of the as-deposited Bi 5 nm film (a),

after thermal annealing up to 525 K (b), after annealing with femtosecond laser pulses at a fluence of $\sim 0.8 \text{ mJ/cm}^2$ with 1 kHz repetition rate (c), and thermally annealed at 450 K while simultaneously being exposed to the laser pulses (d). The diffraction patterns were taken at room temperature. Neither laser annealing nor thermal annealing alone changed the morphology of the two-dimensional islands into nanoclusters. Rather, simultaneous thermal annealing of the grown Bi while exposing it to femtosecond laser pulses resulted in nanocluster formation due to melting and subsequent quenching of the melt. The length distribution of the major axis and the minor axis of the nanoclusters shown in Fig. 1(d) were found to be 16 and 14 nm, respectively, as shown in Fig. 2.

For the as-deposited sample, the Bragg peak (110) is much more intense than the other observed peaks, which reflects a preferred growth orientation. Upon tilting the sample a few degrees off the normal incidence of the electron beam with respect to the sample surface, an arcliffe

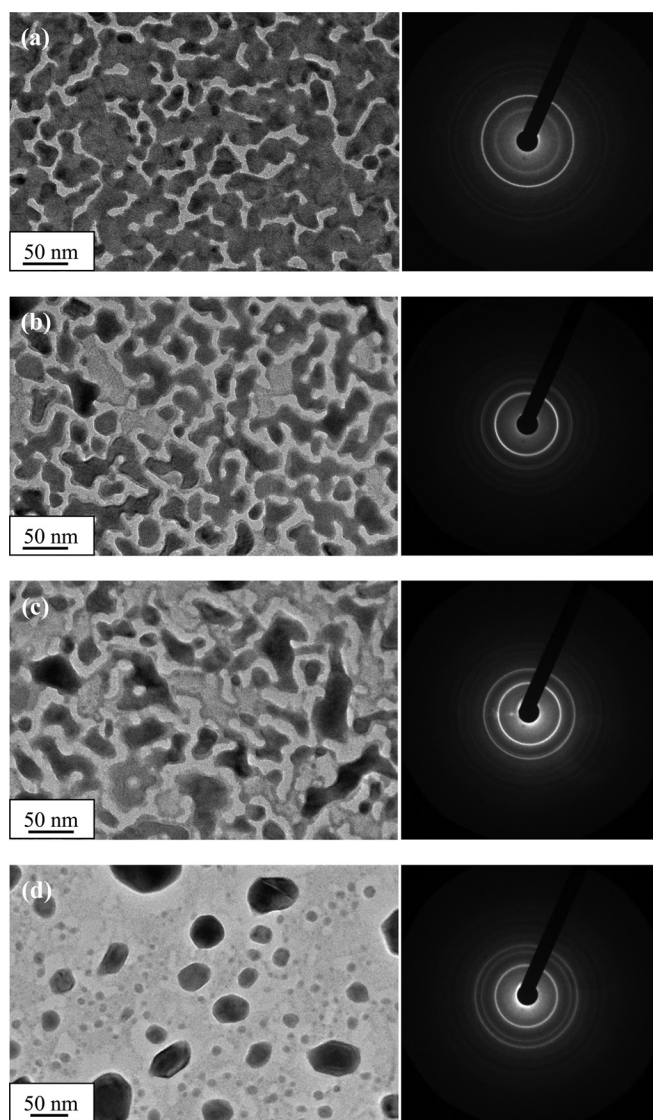


FIG. 1. Transmission electron microscopy and diffraction patterns of Bi: (a) the as-deposited islands, (b) thermally annealed islands, (c) femtosecond laser annealed islands, and (d) simultaneously annealed thermally and with femtosecond laser pulses resulting in formation of nanoclusters.

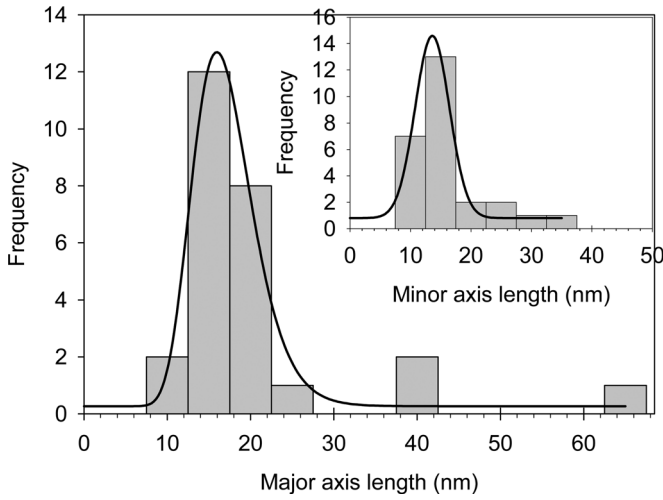


FIG. 2. Major axis and minor axis length distributions of Bi nanoclusters corresponding to samples shown in Fig. 1(d).

diffraction pattern is observed, which indicates the fiber texture of the as-evaporated Bi film. With annealing, there are no observed new Bragg peaks in the diffraction patterns, shown in Figs. 1(b)–1(d). However, the intensity of the Bragg peaks changed. This indicates that annealing did not change the structure of the grown sample, but caused reorientation. The Bragg diffraction rings were identified, as shown in Fig. 3, and they all belong to the hexagonal Bi structure, which precludes the presence of oxide. Figure 3(b) shows the intensity of the diffraction rings as a function of the momentum transfer $S = 2 \sin \theta / \lambda$ (\AA^{-1}) obtained after radial averaging of the Bragg diffraction intensity in Fig. 3(a). Comparison of the diffraction intensity before and after annealing confirms crystal reorientation with annealing. An aluminum thin film was used for calibration of the diffraction camera length. The simple hexagonal structure with lattice parameters of $|a| = |b| = 4.54 \text{ \AA}$ and $|c| = 11.80 \text{ \AA}$ was used to identify the ring pattern of the samples.

High-resolution transmission electron microscopy images of as-deposited and annealed samples are shown in Figs. 4(a) and 4(b). The as-deposited samples show flat islands, while those annealed thermally and simultaneously with the laser show nanoclusters. We will refer to these samples as nanoclusters. Multigrains are observed in some of these nanoclusters, as shown in the high-resolution TEM images in Fig. 4(b).

The Bi lattice parameters a and c and the unit cell volume V were calculated from Eqs. (1)–(3):

$$a = 2d_1d_2 \sqrt{\frac{l_1^2(h_2^2 + h_2k_2 + k_2^2) - l_2^2(h_1^2 + h_1k_1 + k_1^2)}{3(d_1^2l_1^2 - d_2^2l_2^2)}}, \quad (1)$$

$$c = d_1d_2 \sqrt{\frac{l_1^2(h_2^2 + h_2k_2 + k_2^2) - l_2^2(h_1^2 + h_1k_1 + k_1^2)}{d_2^2(h_2^2 + h_2k_2 + k_2^2) - d_1^2(h_1^2 + h_1k_1 + k_1^2)}}, \quad (2)$$

$$V = a^2c \sin \gamma, \quad \gamma = 120^\circ, \quad (3)$$

where, d_1 and d_2 are the interplanar spacing and (h_1, k_1, l_1) and (h_2, k_2, l_2) are Miller indices.³⁴ The values obtained are $a = 4.6 \pm 0.1 \text{ \AA}$, $c = 11.6 \pm 0.1 \text{ \AA}$, and $V = 210.7 \pm 11.2 \text{ \AA}^3$

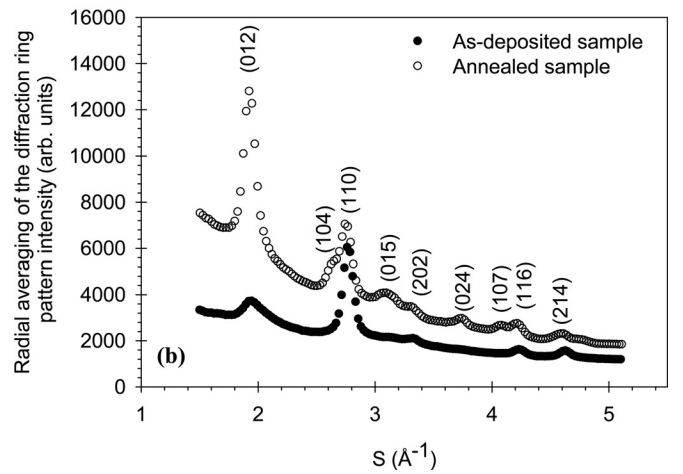
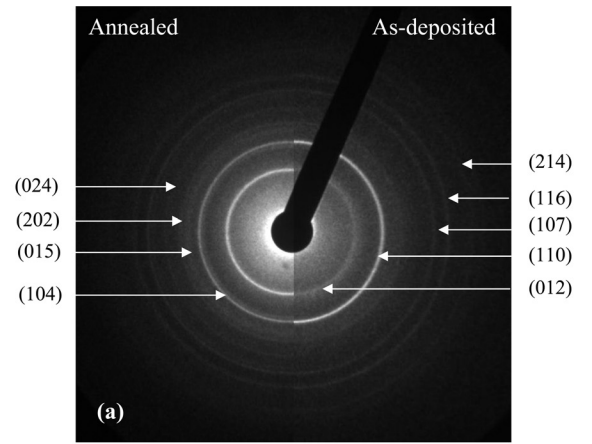


FIG. 3. (a) Diffraction pattern of Bi as-deposited islands and the annealed nanoclusters with Bragg peak identification. (b) Intensity of Bragg peaks as a function of the momentum transfer $S = 2 \sin \theta / \lambda$ (\AA^{-1}) obtained after radial averaging the diffraction ring pattern in (a) and applying Gaussian fitting to obtain the intensity, position, and FWHM of each peak.

in agreement with the parameters reported elsewhere.³⁵ The calculated value of c is less than the reported value for bulk Bi, which can be attributed to the stress imposed on the crystal lattice by the surface tension of the surface atoms in the nanoclusters.

B. Debye–Waller factor

The root mean square displacement of the atoms is directly related to the intensity of the Bragg peak through the Debye–Waller factor:

$$I(G, T) = I_0(G, T) \exp(-2M_G), \quad (4)$$

where $G = \hbar(k_f - k_i)$ is the momentum transfer vector of the scattered electrons,³⁶ and the exponential term is the Debye–Waller factor, where

$$2M_G = \langle u_G^2 \rangle \frac{16\pi^2 \sin^2 \theta}{\lambda^2}. \quad (5)$$

λ is the electron wavelength, θ is the scattering angle, $I_0(G, T)$ is the scattered intensity of a rigid lattice, and $\langle u_G^2 \rangle$ is

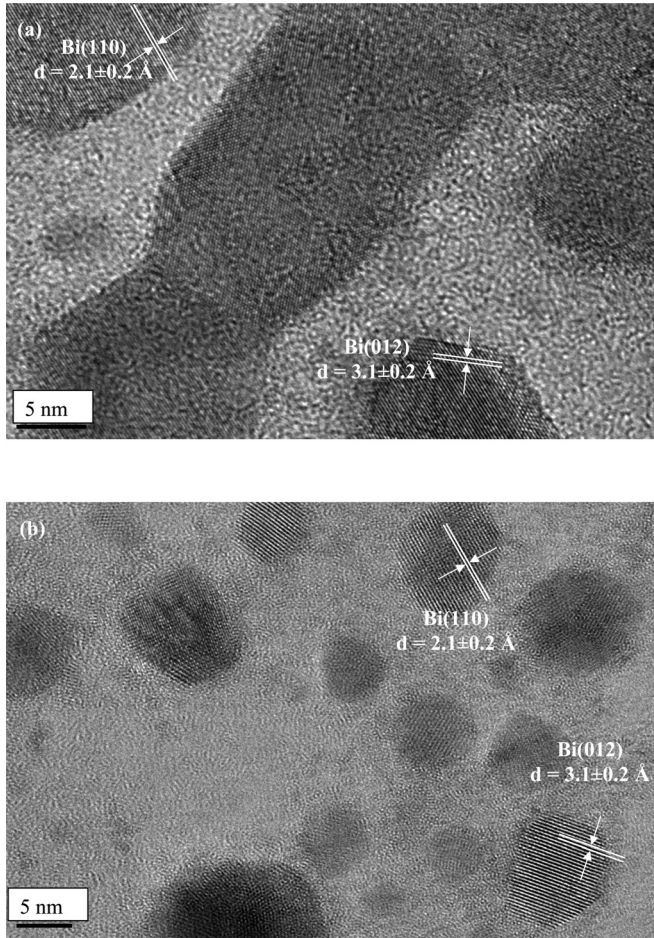


FIG. 4. (a) High-resolution TEM image of as-deposited sample which is thermally evaporated on a TEM grid coated with 10 nm carbon film. (b) High-resolution TEM image of the nanoclusters in Fig. 1(d). The (012) and (110) plane orientations are indicated.

the root-mean-square (rms) vibrational amplitude in the direction of the scattering vector G . The rms vibrational amplitude can be calculated using the harmonic oscillator model in the high-temperature limit,^{37,38}

$$\langle u_G^2 \rangle = \left(\frac{3Nh^2T}{Mk\Theta_D^2} \right), \quad (6)$$

where Θ_D is the Debye temperature, M is the atomic weight of the sample, T is temperature, N is Avogadro's number, k is Boltzmann's constant, and \hbar is Planck's constant divided by 2π . Therefore, from the diffraction intensity dependence on the temperature, we can estimate Θ_D of Bi nanoclusters.

Figure 5 shows the temperature dependence of the Bragg peak intensity normalized to that at $T=323$ K. This measurement was performed on nanoclusters similar to those shown in Fig. 1(d). To estimate the instrumental error in intensity measurement, we measured the intensity of the diffraction ring pattern at room temperature for over ~ 60 min. We found that the intensity fluctuation did not exceed 5%. Results also showed that the recrystallized Bi nanoclusters were not affected by successive heating and cooling cycles and the diffraction peak intensity of recrystallized nanoclusters decays with temperature according to the Debye–Waller

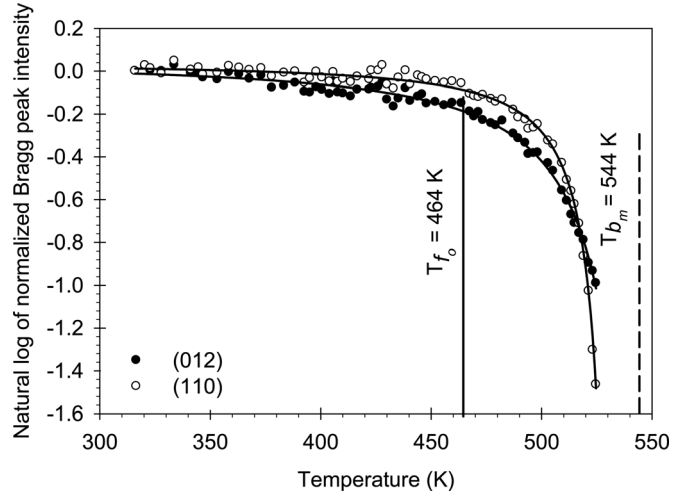


FIG. 5. Temperature dependence of the natural log of intensity normalized to that at temperature = 323 K, (I_T/I_0), of the (012) and (110) Bragg peaks of Bi nanoclusters similar to those shown in Fig. 1(d).

factor up to $T=464 \pm 6$ K, as shown in Fig. 5. The temperature-dependent natural log of the normalized Bragg peak intensity up to $T=464$ K was used to calculate the Debye temperature of the Bi nanoclusters and found to be $\Theta_D = 53 \pm 6$ K as calculated from the (012) diffraction order. This value is consistent with the reported Debye temperature of Bi thin film, $\Theta_D = 42.0 \pm 9$ K,³⁹ and 47 ± 5 K,⁴⁰ which is less than that for the bulk $\Theta_{D,B} = 120$ K. Since the atoms in reduced dimensionality have a less coordination number than surface atoms and, consequently, have thermal vibrational amplitudes greater than that of the bulk, it is expected that Θ_D (nanoclusters) $< \Theta_{D,B}$. The Debye temperature calculated from the (110) diffraction order was found to be 86 ± 9 K. The direction-dependent Debye temperature reflects the anisotropic nature of Bi. The reduced Debye temperature calculated from the (012) diffraction order compared to that from the (110) is indicative of the weaker atomic bonding in the [012] direction.

C. Bragg peak position

The Bragg peak position r is related to the interplanar spacing d for the set of planes producing the Bragg peak. Therefore, the relative change of the Bragg peak position ($\Delta r/r$) measured in the diffraction pattern equals the relative change of lattice plane spacing ($\Delta d/d$) according to Bragg's Law.

The temperature dependence of ($\Delta d/d$) for Bi (012) and (110) planes is shown in Fig. 6. The data presented in Fig. 6 show a crossover in lattice spacing of Bi (012) planes over the temperature range of $T \sim 499$ –511 K. At $T \sim 499$ K, the thermal expansion coefficient α in the [012] direction changes from $+14.4 \pm 2.9 \times 10^{-6} \text{ K}^{-1}$ to $-0.8 \pm 0.3 \times 10^{-3} \text{ K}^{-1}$, showing lattice contraction, rather than expansion, near melting. On the other hand, the Bi (110) planes did not show any abnormal behavior up to 525 ± 6 K with thermal expansion coefficient of $13.7 \pm 2.5 \times 10^{-6} \text{ K}^{-1}$. Although the data presented in Figs. 5–7 are for one scan, all results were the average of six different scans. The error in each calculated value is the standard deviation calculated from those scans.

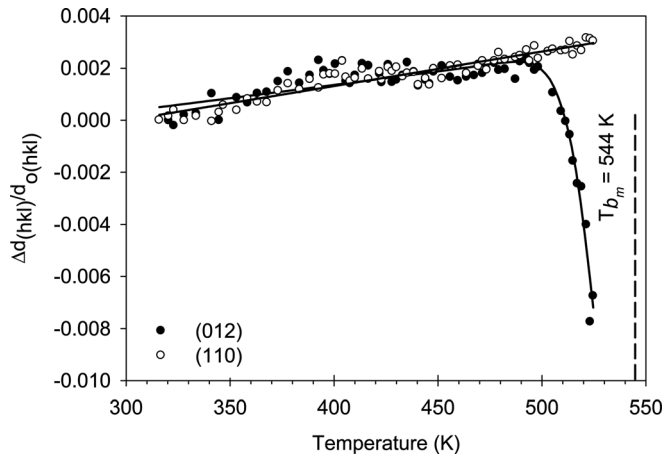


FIG. 6. Temperature-dependent strain of the Bi(012) and Bi(110) planes.

The thermal expansion coefficient of nanocrystals is known to depend on their size and is larger with the reduction of size.⁴¹ Moreover, experimental and theoretical studies showed that the lattice expansion is induced by the excess volume at grain boundaries due to the relatively disordered arrangements of the atoms.⁴² The nanocluster studied here have a size distribution as shown in Fig. 2. Also, some nanoclusters have multigrains. The measured change in the lattice thermal expansion coefficient is that of the distribution of the nanoclusters since diffraction experiments cannot distinguish between the different compositions of the nanocluster distribution.

Many factors may compete and result in such anomaly observed in the Bi(012) direction. Some of these factors are surface stress, surface phonons, defects, as well as finite size effect on the lattice potential.^{33,43} Also, structural phase transitions can lead to similar behavior, but it was ruled out in our case, since the lattice preserves its structure and no extra diffraction rings were observed up to the complete melting of the nanoclusters. The negative expansion coefficient, as observed in Fig. 6, was previously explained in terms of the effect of electronic excitation on the equilibrium lattice spacing.^{33,43}

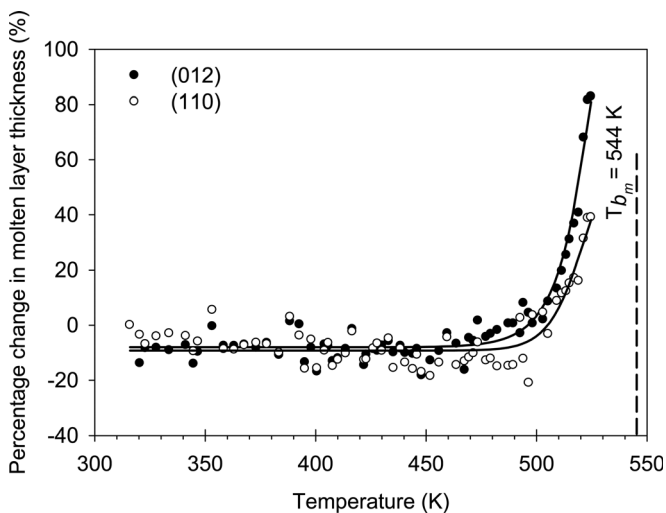


FIG. 7. Temperature dependence of the percentage change in the molten layer thickness, calculated from diffraction ring FWHM at temperature T normalized to that at temperature $T = 323$ K.

D. Full width at half maximum

The average full width at half maximum (FWHM) of the diffraction ring pattern of polycrystalline material is related to the crystallite size in a direction parallel to the sample surface, D , through the Debye–Scherrer formula,³⁴

$$D = \frac{0.94\lambda}{B \cos \theta}, \quad (7)$$

where λ is the electron wavelength, B is the Bragg diffraction order FWHM expressed in radians, and θ is Bragg angle. At room temperature, an average crystallite size of 101 ± 10 Å was calculated from Eq. (7) based on the average of six diffraction patterns from different runs.

The reduction in the crystalline size with temperature can be attributed to the formation of liquid shells surrounding the nanoclusters. Figure 7 shows the temperature dependence of the percentage change in the molten layer thickness, calculated from the change in the diffraction ring FWHM at temperature T normalized to that at $T = 323$ K, $\Delta B/B_0$, for (012) and (110) Bragg peaks, where $B(T)$ is the FWHM at temperature T , B_0 is the FWHM at 323 K, and $B = B(T) - B_0$. For temperatures up to ~ 500 K, there is no significant change in the FWHM with temperature for the (110) order, however, some changes in the (012) order appear at a lower temperature and are more significant than that in the [110] direction. For $T > 500$ K, a significant crystallite size reduction is detected due to the formation of a thin layer of liquid Bi around the solid Bi nanocluster, which grows in size as the temperature increases until the nanocluster is fully transformed into the liquid phase.^{15,44} There is an observed anisotropy in the molten layer thickness with that observed in the [012] direction more than in the [110] direction. This result is consistent with the reduced Debye temperature in the [012] direction. A lower Debye temperature is generally associated with reduced melting point.

IV. DISCUSSION

Crystal melting starts at the surface and depends on the crystal facet.⁴⁵ The high-density close-packed surfaces are less energetically favored to be wetted by the melt, while the low-density packed ones can be wetted.⁴⁵ As the crystal temperature approaches the melting point, a quasiliquid layer forms on the less-packed surfaces and, with increasing temperature, the whole nanocluster melts. The quasiliquid layer is a layer of disordered atoms which has stronger bonding than those in the melt. Such melting mechanism necessitates the presence of repulsive forces between the liquid–vapor and liquid–solid interfaces over some distance.⁴⁵

Thermal expansion upon heating occurs in most solid substances, whether they are elements or compounds. This phenomenon is generally due to a force that initiates the thermal expansion and is described by the Grüneisen parameter and the elastic reaction of the solid to this force.^{46,47} This force is usually a thermal pressure induced by the strain produced in the lattice as a result of the increased lattice mean vibrational amplitude as the temperature increases.

Some materials are known to contract upon heating.^{33,34,43} Two main contributions are considered when studying lattice contraction upon heating; namely, the vibrational and

nonvibrational contribution.⁴⁸ For a crystal with anisotropic lattice parameters, contraction along one crystal direction could be accompanied with expansion along another direction.^{49,50} This is due to the impact of the potential energy curve on the crystal direction. Along the direction of high compressibility in the lattice, normal modes of vibrations with high frequencies are excited at a certain temperature at the expense of those with low frequencies.⁴⁸ In this case, contraction in one direction is accompanied by an expansion in the direction perpendicular to it.

The data in Fig. 6 show that a transition from a positive thermal expansion to a negative one for the Bi (012) planes starts at $T \sim 499 \pm 11$ K, with no structural phase transition observed. This anomaly was previously explained in terms of the effect of electronic excitation on the lattice interplanar spacing.^{33,43} In Bi nanoclusters, the energy levels are a few meV apart and, consequently, the potential of the electrons occupying the valence band becomes high enough to affect the lattice atomic positions. Therefore, raising the lattice temperature increases the energy level separation. This leads to a reduction in the number of excited electrons and increases the thermal energy of the already-excited electrons occupying the conduction band. These factors cause the lattice to contract, rather than expand, upon raising its temperature. This, also, may suggest the previous observation of semimetal–semiconductor transition in Bi nanoclusters at a critical thickness of 13 nm,^{24,25,51,52} where the molten layer increases with temperature at the expense of the solid Bi.

V. CONCLUSIONS

Transmission electron diffraction was used to study the structural properties of Bi nanoclusters from room temperature up to 525 ± 6 K. From the temperature-dependent diffraction intensity measurement, the Debye temperature of the annealed nanoclusters was found to be 53 ± 6 K along the [012] direction and 86 ± 9 K along the [110] direction. At $T = 464 \pm 6$ K, the diffraction intensity starts to deviate from the exponential Debye–Waller behavior, which indicates the increased lattice anharmonicity with temperature. In addition to the positive thermal expansion before melting, a lattice contraction starts at $\sim 499 \pm 11$ K, which can result from the disturbance in the potential of the electrons occupying the valence band that affects the lattice atomic positions. The onset of melting of the Bi nanoclusters was estimated from the diffraction linewidth to occur at $T \sim 500 \pm 6$ K. The size of the nanoclusters was observed to be reduced with heating. This observation is interpreted to be due to the formation of a thin liquid shell around the nanoclusters.

ACKNOWLEDGMENTS

This material is based upon work supported by the US Department of Energy, Division of Material Science, under Grant No. DE-FG02-97ER45625 and the National Science Foundation under Grant Nos. DMR-9988669 and MRI-0821180.

¹L. H. Liang, J. C. Li, and Q. Jiang, *Condens. Matter* **334**, 49 (2003).

²R. Goswami and K. Chattopadhyay, *Acta Mater.* **52**, 5503 (2004).

³M. Zhang, M. Yu. Efremov, F. Schiettekatte, E. A. Olson, A. T. Kwan, S. L. Lai, T. Wisleder, J. E. Greene, and L. H. Allen, *Phys. Rev. B* **62**, 10548 (2000).

- ⁴K. M. Unruh, T. E. Huber, and C. A. Huber, *Phys. Rev. B* **48**, 9021 (1993).
- ⁵C. Q. Sun, Y. Wang, B. K. Tay, S. Li, H. Huang and Y. B. Zhang, *J. Phys. Chem. B* **106**, 10701 (2002).
- ⁶G. Kellermann and A. F. Craievich, *Phys. Rev. B* **78**, 054106 (2008).
- ⁷P. R. Couchman and W. A. Jesser, *Nature (London)* **269**, 481 (1977).
- ⁸V. P. Skripov, V. P. Koverda, and V. N. Skokov, *Phys. Status Solidi A* **66**, 109 (1981).
- ⁹R. R. Vanfleet and J. M. Mochel, *Surf. Sci.* **341**, 40 (1995).
- ¹⁰H. Reiss, P. Mirabel, and R. L. Whetten, *J. Phys. Chem.* **92**, 7241 (1988).
- ¹¹K. F. Peters, J. B. Cohen, and Y. Chung, *Phys. Rev. B* **57**, 13430 (1998).
- ¹²T. Castro and R. Reifenberger, *Phys. Rev. B* **42**, 8548 (1990).
- ¹³Y. G. Chushak and L. S. Bartell, *J. Phys. Chem. B* **105**, 11605 (2001).
- ¹⁴E. A. Olson, M. Yu. Efremov, M. Zhang, Z. Zhang, and L. H. Allen, *J. Appl. Phys.* **97**, 034304 (2005).
- ¹⁵M. K. Zayed and H. E. Elsayed-Ali, *J. Appl. Phys.* **99**, 123516 (2006).
- ¹⁶M. K. Zayed and H. E. Elsayed-Ali, *Phys. Rev. B* **72**, 205426 (2005).
- ¹⁷G. L. Allen, R. A. Bayless, W. W. Gile, and W. A. Jesser, *Thin Solid Films* **144**, 297 (1986).
- ¹⁸S. J. Peppiatt, *Proc. R. Soc. London, Ser. A* **345**, 401 (1975).
- ¹⁹L. H. Qian, S. C. Wang, Y. H. Zhao, and K. Lu, *Acta Mater.* **50**, 3425 (2002).
- ²⁰H. Zhang and B. Mitchell, *Mater. Sci. Eng., A* **270**, 237 (1999).
- ²¹J. A. Eastman, M. R. Fitzsimmons, and L. J. Thompson, *Philos. Mag. B* **66**, 667 (1992).
- ²²H. Gleiter, *Nanostruct. Mater.* **6**, 3 (1995).
- ²³C. F. Gallo, B. S. Chandrasekhar, and P. H. Sutter, *J. Appl. Phys.* **34**, 144 (1963).
- ²⁴M. R. Black, P. L. Hagelstein, S. B. Cronin, Y. M. Lin, and M. S. Dresselhaus, *Phys. Rev. B* **68**, 235417 (2003).
- ²⁵Y. Oshima, K. Takayanagi, and H. Hirayama, *Z. Phys. D: At. Mol. Clusters* **40**, 534 (1997).
- ²⁶D. A. Young, *Phase Diagrams of the Elements* (University of California Press, Berkeley, CA, 1991).
- ²⁷J. N. Johnson, D. B. Hayes, and J. R. Asay, *J. Phys. Chem. Solids* **35**, 501 (1974).
- ²⁸R. W. G. Wyckoff, *Crystal Structures* (Interscience, New York, 1960), Vol. 1.
- ²⁹L. D. Hicks, T. C. Harman, and M. S. Dresselhaus, *Appl. Phys. Lett.* **63**, 3230 (1993).
- ³⁰Ph. Hofmann, *Prog. Surf. Sci.* **81**, 191 (2006).
- ³¹F. Jona, *Surf. Sci.* **8**, 57 (1967).
- ³²J. F. van der Veen, B. Pluis, and A. W. D. van der Gon, in *Chemistry and Physics of Solid Surfaces VII* (Springer, Berlin, 1988), pp. 455–490.
- ³³L. Li, Y. Zhang, Y. W. Yang, X. H. Huang, G. H. Li, and L. D. Zhang, *Appl. Phys. Lett.* **87**, 031912 (2005).
- ³⁴B. D. Cullity, *Elements of X-ray Diffraction*, 2nd ed. (Addison-Wesley, Reading, MA, 1978).
- ³⁵X. F. Yu, X. Liu, K. Zhang, and Z. Q. Hu, *J. Phys.: Condens. Matter* **11**, 937 (1999).
- ³⁶D. A. Amis, R. S. Shah, and R. O. Simmons, *Phys. Rev. B* **67**, 094303 (2003).
- ³⁷R. M. Goodman, H. H. Farrell, and G. A. Somorjai, *J. Chem. Phys.* **48**, 1046 (1968).
- ³⁸J. M. Morabito, Jr., R. F. Steiger, and G. A. Somorjai, *Phys. Rev.* **179**, 638 (1969).
- ³⁹E. A. Murphy, H. E. Elsayed-Ali, and J. W. Herman, *Phys. Rev. B* **48**, 4921 (1993).
- ⁴⁰A. Janzen, B. Krenzer, P. Zhou, D. von der Linde, and M. Horn-von Hoegen, *Surf. Sci.* **600**, 4094 (2006).
- ⁴¹R. Banerjee, E. A. Sperling, G. B. Thompson, H. L. Fraser, S. Bose, and P. Ayyub, *Appl. Phys. Lett.* **82**, 4250 (2003).
- ⁴²Y. F. Zhu, W. T. Zheng, and Q. Jiang, *Appl. Phys. Lett.* **95**, 083110 (2009).
- ⁴³W.-H. Li, S. Y. Wu, C. C. Yang, S. K. Lai, K. C. Lee, H. L. Huang, and H. D. Yang, *Phys. Rev. Lett.* **89**, 135504 (2002).
- ⁴⁴H.-P. Cheng and R. S. Berry, *Phys. Rev. A* **45**, 7969 (1992).
- ⁴⁵J. W. M. Frenken and H. M. van Pinxteren, *Surf. Sci.* **307–309**, 728 (1993).
- ⁴⁶E. Gruneisen and E. Goens, *Z. Phys.* **29**, 141 (1924).
- ⁴⁷N. W. Ashcroft and N. D. Mermin, *Solid State Physics* (Saunders College Publishing, Philadelphia, 1976), Chap. 25.
- ⁴⁸G. D. Barrera, J. A. O. Bruno, T. H. K. Barron, and N. L. Allan, *J. Phys.: Condens. Matter* **17**, R217 (2005).
- ⁴⁹A. C. Bailey and B. Yates, *J. Appl. Phys.* **41**, 5088 (1970).
- ⁵⁰B. G. Childs, *Rev. Mod. Phys.* **25**, 66 (1953).
- ⁵¹J. Heremans, C. M. Thrush, Z. Zhang, X. Sun, M. S. Dresselhaus, J. Y. Ying, and D. T. Morelli, *Phys. Rev. B* **58**, R10091 (1998).
- ⁵²Z. Zhang, X. Sun, M. S. Dresselhaus, J. Y. Ying, and J. P. Heremans, *Appl. Phys. Lett.* **73**, 1589 (1998).